GFZ

Helmholtz-Zentrum
POTSDAM

Originally published as:

Check for updates

"On demand" triggered crystallization of CaCO₃ from solute precursor species stabilized by the water-in-oil microemulsion†

Tomasz M. Stawski, ⭐*ab Teresa Roncal-Herrero, ‡c
Alejandro Fernandez-Martinez,d Adriana Matamoros-Veloza, §b
Roland Kröger *c and Liane G. Benning *abe

Can we control the crystallization of solid CaCO₃ from supersaturated aqueous solutions and thus mimic a natural process predicted to occur in living organisms that produce biominerals? Here we show how we achieved this by confining the reaction between Ca^{2+} and CO_3^{2-} ions to the environment of nanosized water cores of water-in-oil microemulsions, in which the reaction between the ions is controlled by the intermicellar exchange processes. Using a combination of *in situ* small-angle X-ray scattering, high-energy X-ray diffraction, and low-dose liquid-cell scanning transmission electron microscopy, we elucidate how the presence of micellar interfaces leads to the formation of a solute CaCO₃ phase/species that can be stabilized for extended periods of time inside micellar water nano-droplets. The nucleation and growth of any solid CaCO₃ polymorph, including the amorphous phase, from such nano-droplets is prevented despite the fact that the water cores in the used microemulsion are highly supersaturated with respect to all known calcium carbonate solid phases. On the other hand the presence of the solute CaCO₃ phase inside of the water cores decreases the rigidity of the micellar surfactant/water interface, which promotes the aggregation of micelles and the formation of large (>2 μm in diameter) globules. The actual precipitation and crystallization of solid CaCO₃ could be triggered "on-demand" through the targeted removal of the organic–inorganic interface and hence the destabilization of globules carrying the CaCO₃ solute.

a German Research Centre for Geosciences, GFZ, Interface Geochemistry, Potsdam,
  Germany. E-mail: stawski@gfz-potsdam.de, benning@gfz-potsdam.de;
  Tel: +49 33128827511, +49 33128828970
b School of Earth and Environment, University of Leeds, LS2 9JT, Leeds, UK
c Department of Physics, University of York, YO10 5DD, York, UK.
  E-mail: roland.kroger@york.ac.uk; Tel: +44 (0)1904324622
d Univ. Grenoble Alpes, Univ. Savoie Mont Blanc, CNRS, IRD, IFSTTAR, ISTerre,
  38000 Grenoble, France
e Department of Earth Sciences, Freie Universität Berlin, Berlin, Germany
† Electronic supplementary information (ESI) available. See DOI: 10.1039/
c8cp00540k
‡ Current address: School of Chemical and Process Engineering, University of Leeds,
LS2 9JT, Leeds, UK.
§ Current address: School of Mechanical Engineering, University of Leeds, LS2 9JT,
Leeds, UK.

Introduction

Calcium carbonate (CaCO₃) is the most abundant functional biomineral in nature. Its mineralization by microorganisms underpins a vast array of Earth system processes, and controls the global carbon cycle.[1] In living organisms metabolic processes regulate the self-assembly pathways and morphologies

of crystalline CaCO₃ phases,[2–4] and key aspects of such CaCO₃ (bio)mineralization reactions have been experimentally reproduced through the use of organic–inorganic interfaces,[5–10] such as the liposomes.[11,12] In particular, reverse micellar systems (water-in-oil microemulsions) have attracted considerable attention in biomimetic studies since they provide a well-defined and tunable organic–inorganic interface ultimately confining the reaction environments to water droplets of just a few nanometers in contrast *e.g.* to the aforementioned liposomes (hence the notion of nanoreactors[7,13]). Because of this confinement and the presence of a surfactant interface, the water molecules within these nano-droplets exhibit slower dynamics in comparison to bulk water.[14,15] Therefore, such water-in-oil microemulsions represent plausible cell membrane analogs.[16,17] Thus they allow for the study of biomineral precipitation reactions in which the formation pathways are controlled by the interface and changes in the physical matrix of the confined reaction medium (*e.g.* water structure), and not by the chemical reactions with the functional organic molecules. Experimentally, this is realized by mixing and diffusive exchange of ions between two separate microemulsions containing

This journal is © the Owner Societies 2018

Phys. Chem. Chem. Phys., 2018, **20**, 13825–13835 | **13825**

distinct dissolved salt ions.[7,16,18–21] For the $CaCO_3$ system, several studies reported that crystalline particles could be obtained and morphologically controlled by mixing microemulsions containing aqueous solutions of CO_3^{2-} and Ca^{2+} at high supersaturation with respect to any solid $CaCO_3$ polymorph.[22–26] In all these studies the underlying assumption was that all observed solid $CaCO_3$ phases and morphologies precipitated directly from the mixed microemulsions, as it was deduced from *ex situ* imaging and analysis of the final reaction products.

However, reverse micelles are inherently dynamic and sensitive to changes in physicochemical properties and solely *ex situ* studies or analysis of final products are insufficient to fully quantify a reaction mechanism at such dynamic organic–inorganic interfaces.[16] Therefore, in the present study we demonstrate how through multi-length-scale *in situ* and time-resolved analyses of bioinspired $CaCO_3$ formed from reverse microemulsions, we gain mechanistic insights into the $CaCO_3$ mineral growth pathways. Using a combination of *in situ* small-angle X-ray scattering (SAXS), high-energy X-ray diffraction (HEXD), and low-dose liquid-cell scanning transmission electron microscopy (LC-STEM), we elucidate how the presence of a micellar interface leads to the formation of a solute $CaCO_3$ phase that is stabilized for extended periods of time inside micellar aqueous nano-droplets. The nucleation and growth of any solid $CaCO_3$ polymorph from such nano-droplets is prevented despite the fact that the water cores in the used microemulsion were highly supersaturated with respect to all known calcium carbonate solid phases. The actual precipitation and crystallization of solid $CaCO_3$ could be triggered "on-demand" through the targeted removal of the organic–inorganic interface. Our data clearly demonstrate that the confinement within a micellar-like environment inside living organisms could be the key factor controlling mineral precipitation at high supersaturation levels.

Experimental

Microemulsion preparation

All experiments were carried out with water-in-oil reverse microemulsion that were equilibrated at 20 °C prior to use. The microemulsions consisted of 0.1 mol L^{-1} dioctyl sodium sulfosuccinate (the surfactant, NaAOT, >98% Sigma Aldrich), dissolved in 2,2,4-trimethylpentane (the oil, isooctane, HPLC grade, Fisher) and water. Typically in our experiments the molar ratio between water and the surfactant was $w = [H_2O]:[NaAOT] = 10$. Two separate initial microemulsions were prepared with water (cores containing either 0.15 mol L^{-1} $CaCl_2$) (hexahydrate, >99%, Fisher), or 0.15 mol L^{-1} Na_2CO_3 (anhydrous, >99.9%, BDH Chemicals Ltd; ultrapure deionized water, MilliQ, resistivity >18 MΩ cm). All the chemicals were used as purchased and without any further purification. The individual, initial unmixed microemulsions, were optically clear and stable for extended periods of time (weeks), but for all experiments fresh microemulsions (maximum 3–4 h old) were prepared. The chemical compositions of the reverse microemulsions used corresponded to a region of the phase diagram,[27] where only reverse micelles

are stable. We also confirmed the stability of the individual unmixed microemulsions by small-angle X-ray scattering analyses (SAXS, see below). Using a $w = 10$ and the above mentioned salt concentrations resulted in individual microemulsions considerably below their water (brine) solubilization capacity ($w_{max} \sim 20$, at [salt] = 0.15 mol L^{-1}, see also ESI,† Note S1). To initiate a reaction we mixed equal volumes of the initial reverse microemulsions containing Ca^{2+} and CO_3^{2-} ions respectively. The mixture yielded a microemulsion of $[Ca^{2+}] = [CO_3^{2-}] = 0.075$ mol L^{-1}. Over the course of ~ 3 h and under gentle stirring at 150 rpm, a translucent whitish colloidal suspension developed and we followed the development of this suspension with time.

Small-angle X-ray scattering (SAXS) characterization

All *in situ* and time-resolved SAXS measurements were carried out at beamline I22 of the Diamond Light Source Ltd (UK). The microemulsions were continuously stirred at 150 rpm in a 200 mL glass reactor, and circulated through a custom-built PEEK flow-through cell with embedded borosilicate capillary aligned with the X-ray beam (ID 1.0 mm, wall thickness ~ 10 μm) using a peristaltic pump (Gilson MiniPuls 3, flow ~ 10 mL min^{-1}). To initiate the reactions we used a secondary peristaltic pump (Gilson MiniPuls 3) as a remote fast injection system. Typically, 15 mL of a Na_2CO_3-containing microemulsion were circulated through the cell and 8 scattering patterns were collected at a rate of 20 s per frame to obtain data for the initial, unmixed microemulsions. While continuing the scattering data collection, we injected 15 mL of a $CaCl_2$-containing microemulsion remotely into the reactor. The injection lasted for ~ 20 s, and no changes in the measured scattering pattern intensities or shapes were observed during injection. The development of the microemulsion mixtures were followed up to ~ 3 h with patterns acquired every 20 seconds. Additionally, we also performed an experiment at a time-resolution of 1 second, in which we injected 10 mL of ethanol (96%) into 50 mL of aged (~ 4 h) $CaCO_3$ microemulsion to study the processes of its destabilization.

The SAXS measurements were performed using a monochromatic X-ray beam at 12.4 keV and two-dimensional scattered intensities were collected at small-angles with a Dectris Pilatus 2M (2D large area pixel-array detector). Transmission was measured by means of a photodiode installed in the beam-stop of the SAXS detector. A typical sample-to-detector distance of 4.27 m allowed for a usable q-range of $0.038 < q < 3.70$ nm^{-1}. We also performed several measurements at 1.2 m and a q-range $0.100 < q < 7.00$ nm^{-1} in order to study fine changes in the structure of micelles. The scattering-range at small-angles was calibrated against silver behenate[28] and dry collagen[29] standards. The scattered intensity was calibrated to absolute units against the 1 mm glassy carbon standard[30] available at I22. The reactions described in the "Microemulsion preparation" section were followed *in situ* from the very early stages and up to the point when no changes in sample transmission were observed (a direct readout from the photodiode) at the time resolution of 20 s per frame. For each of the experiments we measured a series of backgrounds and reference samples, which included: the empty cell, isooctane background, pure-water

13826 | *Phys. Chem. Chem. Phys.*, 2018, **20**, 13825–13835

This journal is © the Owner Societies 2018

microemulsion at w = 10. All recorded 2D SAXS patterns were isotropic and could therefore be reduced to 1D curves. Background subtractions, data corrections, normalizations, and integrations to 1D curves were performed using the DAWN software[31] (v. 1.3 & 1.4) according to I22 guidelines.

In situ liquid-cell STEM/TEM characterization (LC-STEM)

To image the development of the microemulsions containing Ca^{2+} and CO_3^{2-} ions upon mixing, a Protochips Poseidon 200 liquid cell holder was employed. This holder has two injection inlets and one outlet port. The imaging was carried out through two 50 nm thick silicon nitride membranes with a total accessible area of 550 μm × 50 μm separated by a 500 nm spacer. However, it is important to note that the effective fluid thickness is significantly larger due to membrane bowing effects.[32] The membranes were chemically cleaned prior to assembly by rinsing with acetone and ethanol (Sigma Aldrich, ACS reagent grade). To make the silicon nitride membranes hydrophilic a 50 W oxygen plasma was applied for 2 min (Femto, Diener Electronic GmbH). 40 nm × 10 nm gold nanorods (Strem Chemical Inc.) were deposited as fiducial markers onto the top membrane prior to a second plasma treatment. The chips were assembled using a 0.5 μL droplet of the 0.1 mol L^{-1} NaAOT solution in isooctane sandwiched between them to prevent membrane collapse. A pure, 0.1 mol L^{-1} NaAOT solution in isooctane was connected to one liquid cell inlet *via* a 3 mL syringe and PEEK tubing with an internal diameter of 100 μm. The NaAOT solution was continuously pumped through the cell by a syringe pump (Harvard Apparatus Inc.) at a flow rate of 300 μL h^{-1}. Once a stable and focused image was obtained, using the gold nanorods as fiducial markers, a Ca^{2+}-containing microemulsion was pumped through one of the inlets and the CO_3^{2-} containing microemulsion was injected through the second inlet. Both emulsions mixed in the tip volume of the holder. Additionally we also imaged *in situ* each of the salt-carrying microemulsions to check for any presence of globules, and we confirmed that no such morphologies were present, and hence they formed only upon mixing of the two microemulsions. In order to destabilize the as-formed globules and to induce the crystallization of CaCO$_3$, the flow of the ion-carrying microemulsions was stopped, and in their place ethanol (96%) was pumped into the cell at a flow rate of 300 μL h^{-1}. For the analysis and *ex situ* imaging of the mineral phase, which formed after the ethanol injection, the liquid-cell holder was disassembled and the membrane was analyzed using conventional TEM (see below).

To image the mixing and microemulsion reaction dynamics in the LC-STEM cell, a double aberration corrected JEOL JEM 2200FS (S)TEM operated at 200 kV using a high-angle annular dark-field scanning TEM (HAADF-STEM) detector was used. A 12 mrad α semi-angle condenser aperture was used and the lateral size of the probe was approx. 1 Å. Images were recorded employing a K2 camera of a physical resolution of 1024 × 1024 pixels^2 at a dwell-time of 0.5 μs per pixel resulting in a scan time per frame of approx. 0.5 s. Images were recorded at 20k magnification resulting in a single pixel area of 14 × 14 nm^2.

Videos were acquired using the software Camtasia allowing for the capture of live-view images using Digital Micrograph (JEM 2200, JEM 2011) and were down-sampled to 512 × 512 pixels^2 and stored at 2 fps (see Videos S1 and S2 with real-time data; Videos S3 and S4 contain the same data but are sped up 10 times to 20 fps, ESI†). The time-scales in Fig. 2 and 3 in the main text are independent from each other, and in each case 0 seconds marks the onset of a different event. In Fig. 2A "0 s" at the time scale relates to the mixing of the initial microemulsions, in Fig. 2B it marks the relative onset of growth of the tracked objects, whereas in Fig. 3A and B it relates to the initiation of the injection of ethanol into the port of the liquid cell holder. For the post reaction *ex situ* TEM analysis of the mineral phases, a JEOL 2011 was used at a beam current of approx. 5 μA and an acceleration voltage of 200 kV.

For the *ex situ* characterization of the reaction products presented in ESI:† Fig. S5 and Note S3, the mixed Ca^{2+}- and CO_3^{2-}-carrying microemulsions were directly cast onto holey carbon Cu grids (CF200-Cu, Electron Microscopy Sciences). The as deposited and dried samples were analyzed in TEM mode (high-resolution imaging and selected area electron diffraction, SAED) using a FEI Tecnai TF20, with images recorded by a GatanOrius SC600A CCD camera. We characterized the products of reaction of several compositions of the microemulsions with varying w and using variable initial ion-concentrations, and we did not observe any differences in morphologies of the particles formed. Therefore, all the presented images are from the 0.075 mol L^{-1} CaCO$_3$ system of w = 10 after ~3 h from mixing.

High-energy X-ray diffraction (HEXD) characterization

The HEXD measurements were performed on beamline ID15B at the European Synchrotron Radiation Facility (ESRF, Grenoble, France). In order to achieve better signal to noise ratios for the HEXD measurements we centrifuged the mixed but not destabilized microemulsions at 16 000g. Various times were used to evaluate the influence of centrifugation onto the stability of the microemulsion suspension (5–120 min), and typically a time of 15 min was used. We did this in order to enrich the microemulsion with respect to the Ca–CO$_3$-containing globules by increasing their volume fractions. During centrifugation, the system visibly separated, and 98% of the supernatant could be decanted. The structures of this separated supernatant and of the resulting centrifuged solution as well as the centrifuged initial unmixed microemulsions were also tested with SAXS (at I22, see the SAXS measurement description) to evaluate if centrifugation changes the structure. This analysis confirmed that the post-centrifugation supernatant from the mixed microemulsions contained only reverse micelles but no large scattering objects, and the high-q part of the data ($q > 0.2$ nm^{-1}) for the centrifuged samples indicated that the structure of the reverse micelles was not affected by the centrifugation procedure (see ESI:† Fig. S2). The as-prepared samples were transferred into 1 mm Kapton capillaries, and HEXD analyses were carried out at the wavelength of 0.14383 Å allowing us to collect scattering in the q range up to ~250 nm^{-1}. The 2D HEXD patterns were collected using a MARCCD165 detector (pixel size 150 × 150 μm^2)

This journal is © the Owner Societies 2018

Phys. Chem. Chem. Phys., 2018, **20**, 13825–13835 | **13827**

in Debye–Scherrer geometry according to the ID15B guidelines. The sample-to-detector distance was 234.4 mm and was calibrated using a CeO_2 standard in 1 mm Kapton capillary. Due to the expected relatively low signal-to-background from the measured samples, we used long counting times (up to 200 s, typically 100 s) and collected multiple frames (up to 300 per sample, typically 20), which were later averaged together. The detector dark-current image was measured every 5 frames and dark-current contributions were corrected automatically by the acquisition software. Furthermore, various background and reference samples were measured under similar conditions, and included among others, an empty Kapton capillary, a capillary containing pure isooctane, and powders of solid $CaCO_3$ phases. The as obtained 2D images were transformed into 1D curves using Fit2D[33] from which the atomic pair distribution functions (PDFs) were obtained by using PDFgetX3 software package.[34] The background and Compton scattering subtractions were also performed using the same software package.

Results

Mixing and diffusion between two microemulsions

We started our experiments with two initially clear reverse micro-emulsions containing 0.15 mol L^{-1} $CaCl_2$ and 0.15 mol L^{-1} Na_2CO_3 solutions in the water cores. Analyzing these initial non-mixed single salt reverse micelles by SAXS revealed water cores with an average diameter of $\sim$3.4 nm. Including the surfactant film this resulted in a total diameter of the reverse micelles of $\sim$7 nm (see ESI:† Note S1, Fig. S1, Table S1 and ref. 35). Furthermore, our SAXS data confirmed that the chemistry of the dissolved salts in the aqueous cores, did not affect the size or shape of the micellar water pools (ESI:† Fig. S1). After characterizing the individual microemulsions we mixed equal volumes of the two initially clear Ca^{2+} and CO_3^{2-} containing micro-emulsions, resulting in an equivalent of 0.075 mol L^{-1} $CaCO_3$ in the aqueous sub-phase. Based on previous work,[20,22,23] this "bulk" mixed solution is predicted to exchange Ca^{2+} and CO_3^{2-} ions between the water cores of the two micelles, and thus create an aqueous phase supersaturated with respect to all solid $CaCO_3$ phases (see ESI:† Experimental for the respective saturation indices). We followed and quantified the evolution of such mixed systems through *in situ* and time-resolved SAXS experiments for up to 180 min. Our results (Fig. 1) revealed that at high scattering vector magnitudes, $q > 0.2$ nm^{-1}, the SAXS patterns were dominated by scattering from the core–shell droplets[35,36] of the reverse micelles and that this high-q region was practically identical to scattering patterns of the non-mixed single salt micelles (see ESI:† Fig. S1 and Table S1). Analyzing the change in scattering in this high-q region and utilizing the $I(q)q^4$ *vs.* q representation (inset in Fig. 1) allowed us to show that the average volumes of the water cores of the individual micelles decreased by approx. 5%, indicating only a minor change in the chemical environment inside the micelles. In contrast, a major ($\sim$500%) increase observed in the scattering intensity at $q < 0.2$ nm^{-1} during the first 90 min, indicated
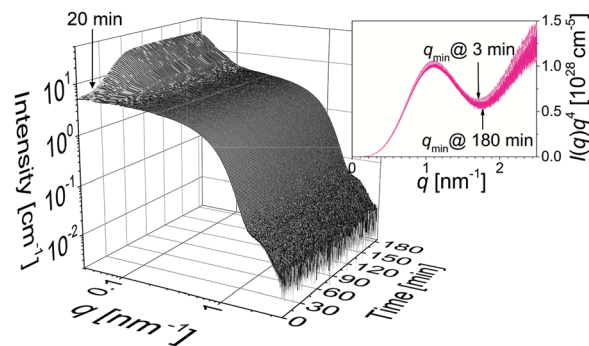

Fig. 1 *In situ* and time-resolved SAXS patterns from a mixed $CaCO_3$ microemulsion. The first 8 frames (up to 2 min and 40 s) correspond to a pure CO_3^{2-}-microemulsion, after which a Ca^{2+}-carrying microemulsion was injected. Between the moment of mixing and up to $\sim$20 min (arrow) no difference between the single-component system and the mixed system was observed; following this the gradual increase in intensity at $q < 0.2$ nm^{-1} up to 90 min indicates the formation of large scattering objects; furthermore, at $q > 0.2$ nm^{-1} changes in the scattering patterns (intensity and shape; see inset $I(q)q^4$ *vs.* q time resolved plot) translated into a minor ($\sim$1.5%) decrease in an average micellar radius (see arrows in inset pointing to the shift in position of the first minimum in the plot (q_{min}) towards higher-q, where the total average radius of the micelle is $\sim$4.5/q_{min}). This change translates into a $\sim$5% volume reduction of the micellar water cores when the constant size of the surfactant polar heads is taken into account.

attractive interactions between the individual micelles,[35,37,38] and this pointed to the gradual development of larger scattering objects. After $\sim$90 min no further change in the system was observed indicating that these large objects became relatively stable. The dramatic low-q increase in intensity and the fact that at $q > 0.2$ nm^{-1} the scattering curves from the freshly mixed (*e.g.*, 3 min) and the aged system (*e.g.*, 180 min), were identical within the experimental uncertainty, can be best explained as the result of clustering of the initially nano-sized, individual reverse micelles into large objects which are themselves embedded in a "sea" of non-clustered micelles. This indicates that in the mixed system the total population of individual small micelles remained fixed over time, yet the arrangement is space of the individual micelles changed over time leading to the formation of the large aggregated clusters of micelles. The shape of the scattering patterns at $q < 0.2$ nm^{-1} also indicates that after $\sim$20 min (arrow in Fig. 1) the size of the individual, large aggregated objects grew very rapidly to diameters >150 nm and thus fell outside the detectable q-range *i.e.*, once the intensity started increasing at low-q practically no Guinier plateau in the $I(q) \propto q^0$ region was observed. Hence, the continuous increase in scattering intensity between 0 and 90 min originated primarily from the growing number density of these large aggregated objects and not from their gradual growth in size. This interpretation is further evidenced by the SAXS measurements of $CaCO_3$ micro-emulsions centrifuged to the point that 98% of the supernatant was removed (see ESI:† Fig. S2A and Experimental). This procedure was intended to considerably increase the contribution of the large aggregated objects to scattering with respect to the "sea" of the non-clustered micelles. This effect was visible
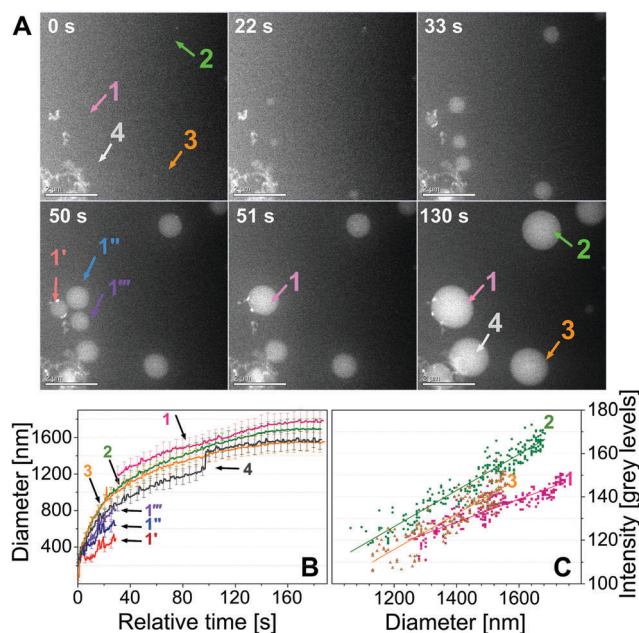
13828 | *Phys. Chem. Chem. Phys.*, 2018, **20**, 13825–13835

This journal is © the Owner Societies 2018

by a shift of the low-q intensity increase region (see the arrow in ESI:† Fig. S2A) from $q < 0.2$ nm^{-1} (the non-centrifuged case) to $q < 0.4$ nm^{-1} (the centrifuged case). We point out that, at the same time the centrifugation procedure did not affect the form factor part of the profile ($q > 0.4$ nm^{-1}), which was identical to the final stage of aggregation of micelles.

Direct *in situ* imaging of the gradual formation of the micellar clusters

To directly image in real space the formation and growth of the large objects (>150 nm) characterized above from the SAXS measurements in reciprocal space, we employed time-resolved and *in situ* LC-STEM approach. Indeed, in Fig. 2A selected time-resolved images extracted from ESI:† Video S1, document the

Fig. 2 The evolution of globules as observed in LC-STEM. The images were obtained at a low electron beam current (4 pA), which minimized the electron dose reducing it by orders of magnitude compared to plane-wave illumination in TEM. This allowed us to image at low dose values of 3 e nm^{-2} at the chosen magnification, and enabled us to minimize electron beam related artefacts. In the field of view, an individual pixel corresponded to approx. 14×14 nm^2, thus not allowing for the imaging of individual reverse micelles. We observed the formation of large globules only following the mixing of the Ca^{2+}- and CO$_3^{2-}$ carrying microemulsions inside the liquid-cell, and never when we only imaged the initial non-mixed salt-carrying microemulsion. A–C are derived from Video S1 (ESI†); in A the time scale corresponds directly to that of the video's, whereas in B the time scale represents a relative growth periods as each of the tracked objects, which started developing after certain induction periods. (A) Selected unprocessed images from the growth sequence of several globules marked 1–4; object 1 was formed from three smaller units 1′–1‴ that grew independently of each other until the 50th s; objects 2, 3 and 4 grew gradually (except that object 4 increased in size by 20% within 1 frame after 100 s of its relative growth time) – see (B); interestingly all tracked globular objects reached similar maximum sizes of ~1600 nm (B) change in diameters of tracked objects 1–4 as a function of time; (C) correlation between diameters of objects 1–3 from the selected time series, and the recorded transmission intensity; colored symbols and lines used in B and C, correspond to the objects 1–4 indicated by the same colors in A.

formation of globular objects (labeled 1–4 in Fig. 2A), which match the large aggregated objects observed in SAXS. In the LC-STEM images, the observed globules far exceed in size both the dimensions of the initial individual reverse micelles (diameter ~ 7 nm), and the maximum size observable in SAXS (>150 nm), since in the LC-STEM observations the imaged globules reached a radius of approx. 900 nm several minutes after the onset of their growth (Fig. 2B). Interestingly, in the LC-STEM experiments the formation of the globular structures appears to be significantly faster than in our scattering experiments (Fig. 1). However, with SAXS we measured the overall progress of the reactions, and showed that the change in scattering intensity reflected a combination of the growth rate of individual globules and the global "rate of appearance" of new globules (*i.e.*, the increase of their number density, see also ESI:† Note S2). The time-resolved LC-STEM images within which we follow 4 tracked objects revealed that these started to form only after mixing of the two microemulsions in the liquid-cell ($t = 0$ s in Fig. 2A). This shows that the globular objects formed through the interaction between the two individual salt-carrying micelles upon mixing. Importantly, the globules were soft, nearly spherical and liquid-like in nature *i.e.* they exhibited high diffusion rates. This is clearly illustrated by the growth of objects 1′–1‴ (Fig. 2A), which merged into a new spherical object 1 within a single frame during the *in situ* imaging. The liquid-like properties were further evidenced by the fact that large globules could expand near-instantaneously (within a single frame – Fig. 2B) at the expense of smaller ones. For example, tracked object 4 in Fig. 2A revealed that it expanded its radius after 100 s of growth (relative time) by 20% (sharp increase in diameter; Fig. 2B) through the rapid merging with/of several smaller neighboring globular objects. The growth profiles of the individual globular objects yielded comparable sizes as a function of relative growth time (Fig. 2B), indicating the relative homogeneity of the physicochemical conditions within the field of view (Fig. 2A). Considering that the diameters of the globules were in fact larger than the 500 nm spacer between the Si$_3$N$_4$ windows of the liquid-cell system (Fig. 2 and ESI:† Experimental), leads to the question as to what extent the confined environment between the Si$_3$N$_4$ windows affected the growth of the globules (see also ESI:† Note S2)? If the confinement played a major role, the globules should become either lens-shaped, or, depending on the wetting between the globules and the Si$_3$N$_4$ membrane, be truncated as they grow and reach the opposite-faced membrane. To distinguish between these two possibilities, we correlated the cross-sectional diameters of globules 1–3 (Fig. 2A), with the corresponding transmission intensities corrected for the temporal background levels (Fig. 2C), revealing a linear dependence between globule sizes and intensity. This correlation suggests that the globules remained spherical in shape even if their diameters grew larger than the 500 nm of the spacer and despite the apparent confinement further indicating that the overall fluid layer thickness inside the liquid cell was significantly larger than 500 nm. This can be explained by the fact the Si$_3$N$_4$ membranes are not stiff and can bow, allowing for

membrane-liquid interactions at locally larger distances.[32] It is important however, that all globules grew at equivalent rates (Fig. 2B) and reached a similar size plateau with diameters just under ~ 2 μm. We conclude that this value corresponds to the actual local distance between the membranes within the field of view. Thus, it seems that the growth of the globules was clearly restricted upon reaching the hydrophilic surface of the opposite Si_3N_4 window. Combined, the spherical shape of the globules and their restricted final sizes imply that the contact angle between the globules and the membrane is very high, pointing to a low affinity between the hydrophilic membranes and the developing structures. In turn this confirms that the globular objects are hydrophobic in nature, which is due to the presence of terminating hydrophobic tails from the surfactant at the surfaces of globules (ESI:† Fig. S1). This matches the expected behaviors for clusters of aggregated reverse micelles as derived above from the SAXS data.

Combining the LC-STEM and SAXS analyses suggests that the globular objects grew by aggregation/clustering of individual reverse micelles. Furthermore, once the globular aggregates of micelles reached a plateau, they stopped growing and remained stable (Fig. 1A and 2B). However and most significantly, in none of the analyses above did we observe any solid or particulate morphologies (*e.g.* ref. 23, 24 and 39–42) that would suggest the formation of either crystalline $CaCO_3$ or amorphous calcium carbonate (ACC) solid phases. Therefore, based on our observation we can assert that in our mixed microemulsion system we have no solids, despite the fact that we are locally highly supersaturated with respect to all $CaCO_3$ phases.

In situ and time-resolved crystallization

To assess if and how the as-formed aggregated globular structures can crystallize, we induced a change in the composition of the microemulsion environment through the injection of ethanol into the liquid cell. This lead to an immediate destabilization and disintegration of the globules and the subsequent, almost instantaneous, formation of a solid phase (Fig. 3A, ESI:† Video S2). We quantified the formation kinetics of this new phase using the cross-sectional area of particles within the field of view as a proxy (ESI:† Fig. S3A). In the first stage of reaction (up to 50 s), the globules instantaneously disintegrated once they came into contact with the passing alcohol front, or even before due to the mixing between the ethanol and isooctane in the cell (compare Fig. 3A at 0 s and the decrease in area and change in shape of the globules at 30 and 50 s, ESI:† Fig. S3A). Once disintegrated, the growth of a new phase occurred and it followed a sigmoidal dependence, until nearly the entire field of view was filled with this phase (ESI:† Fig. S3A). The newly crystallized phase grew into dendritic-like structures. We used *ex situ* TEM analysis of the phase that grew on the Si_3N_4 windows and show that two types of features formed (i) large dried and burst globular objects, made of fan/flower like shapes (ESI:† Fig. S3B), and (ii) large dendritic structures that extended for tens of microns across the window (ESI:† Fig. S3C). These fan and dendrite morphologies formed under flow conditions and in the confined space of the liquid cell (Fig. 3 and ESI:† Fig. S3A)
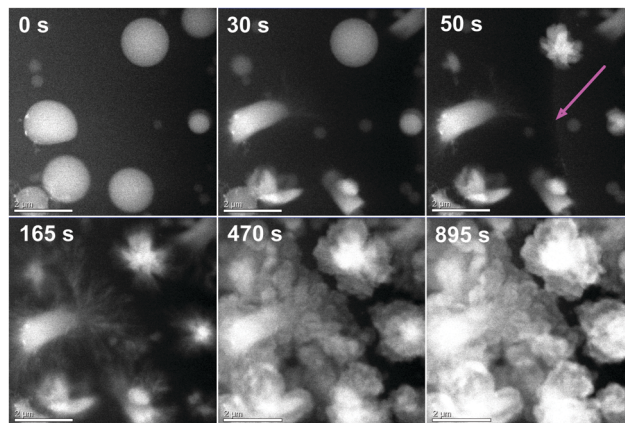
Fig. 3 Destabilization of the $CaCO_3$ microemulsion. Selected unprocessed images from the destabilization sequence of globules as observed by LC-STEM upon *in situ* ethanol injection into the cell taken at 3 e nm^{-2}; the purple arrow in the frame at 50 s points to the contrast change caused by the passing ethanol front; note however, that the burst of the 1st globule was already visible at <30 s; the dynamics of the reaction is better seen in Video S2 (ESI†); the time scale correspond to that in the Video S2 (ESI†), where $t = 0$ s marks the injection of ethanol after the image sequence in Video S1 (ESI†) had been taken.

and based on the *ex situ* TEM analyses (ESI:† Fig. S3C) were determined to be crystalline. The nature of this *in situ* formed mineral phase was revealed by selected area electron diffraction to be the $CaCO_3$ polymorph vaterite (ESI:† Fig. S3D, S4, S5, Table S2 and Note S3). The *in situ* SAXS from the $CaCO_3$ microemulsion measured during the analogous ethanol injection in bulk (ESI:† Fig. S2B and C) showed that the destabilization at the nanometre-scale involved a total disruption of the micellar structure, where the intensity at $q > 0.2$ nm^{-1} decreased by a factor of ~ 10 times, as the form factor of the micelles had completely disappeared.

Do the globular aggregates contain solid calcium carbonate before the induced crystallization?

Over the course of our investigations the fundamental question arose, whether the mixed microemulsions that formed the globular aggregates contained solid calcium carbonate phases before the globules were destabilized. In order to answer this we performed *in situ* HEXD analyses on the aged (~ 4 h) $CaCO_3$ microemulsion containing globules. From these HEXD measurements, we derived the pair distribution function $g(r)$ (PDF; Fig. 4A) of the globules, which we compared to the PDFs of various solid $CaCO_3$ phases and the independent components of the microemulsion. The $g(r)$ of the aggregated globular $CaCO_3$ microemulsion (A) was different from the actual microemulsion components (Fig. 4B and C) and showed a characteristic and unique peak at 2.46 Å, which was attributed to a Ca–O distance.[43] This value lies between the Ca–O bond distance in the $g(r)$s in solid amorphous calcium carbonate (ACC; 2.39 Å; Fig. 4D) and aragonite (2.51 Å; Fig. 4G). However, and importantly, compared to any of the solid samples analyzed (patterns D to G) the structural coherence in the microemulsion sample (A) did not extend above ~ 4 Å, which is characteristic
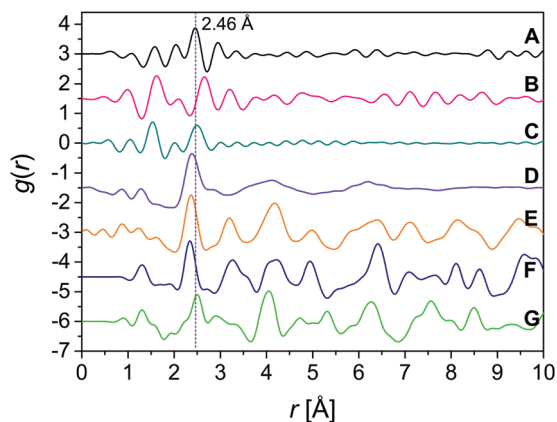
13830 | *Phys. Chem. Chem. Phys.*, 2018, **20**, 13825–13835

This journal is © the Owner Societies 2018

Fig. 4 Atomic PDFs of the aggregated globular $CaCO_3$ microemulsion compared to microemulsion components and standard solid $CaCO_3$ polymorphs. (A) A centrifuged 0.075 mol L^{-1} $CaCO_3$ microemulsion at $w = 10$ (with isooctane background subtracted); the $g(r)$ shows a characteristic unique peak at 2.46 Å and no structural coherence above ~ 4 Å. The peak can be attributed to a Ca–O distance;[43] (B) surfactant component of the microemulsion: 0.1 mol L^{-1} NaAOT solution in isooctane with the medium subtracted as a background; (C) oil component of the microemulsion – pure isooctane; (D) solid amorphous calcium carbonate (ACC); (E) crystalline vaterite; (F) crystalline calcite; (G) crystalline aragonite; PDFs D–G were measured using dry powder samples. A characteristic "rippling" in patterns A to C at $r > 4$ Å is an artifact of the Fourier transform of the as-collected HEXD data and is a consequence if decreased signal-to-noise ratios in liquid samples compared to dry powdered samples shown in D–G.

for liquids (for instance Fig. 4C). Such short coherence suggests that the analyzed mixed and aggregated $CaCO_3$ microemulsion globules contained only solute Ca–CO_3 species and not an amorphous (D) or crystalline solid $CaCO_3$ phase (E, F and G in Fig. 4). Furthermore, our SAXS characterization of both non-centrifuged and centrifuged aged $CaCO_3$ microemulsions (compare Fig. 1 and ESI:† Fig. S2) points out to no morphological changes to the microemulsion at high-q. That means that no species were present, which would have a form or electron density different than the micelles themselves.
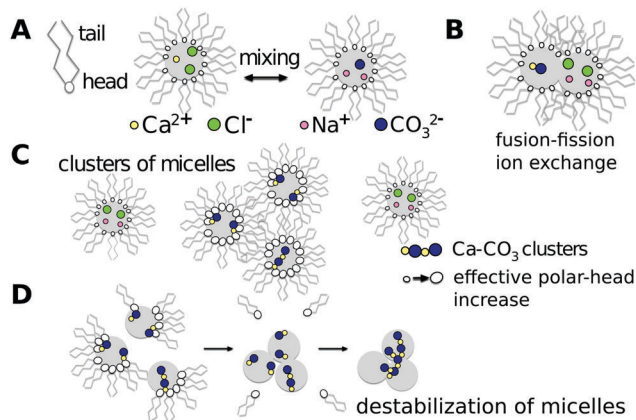
Discussion

When the reverse micelles collide, due to the attractive forces and the fluidity of the dynamic surfactant films, they fuse to transitional clusters, exchange their water cores' contents (e.g., ions) and then again separate (fusion–fission mechanism[18,20]). This communication is an intrinsic property of microemulsions. In our system, the inter-droplet Ca^{2+} and CO_3^{2-} exchange enables interaction and exchange between the individual reverse micelles. Such chemical communication and exchange should invariably lead to supersaturation with respect to calcium carbonates inside the water nanoreactors and thus this should trigger precipitation of a solid phase. Why does no solid $CaCO_3$ phase form/precipitate, and why do these micellar communications instead lead to the formation of large and stable aggregated globules?

In our experiments, the diameters of the water cores in the initial, separated reverse micelles were in the range of 3–4 nm

(ESI:† Fig. S1). This means that at the initial, nominally high Ca^{2+} and CO_3^{2-} concentration of 0.15 mol L^{-1}, each water core contained on average only ~ 1–3 ions of calcium or carbonate (in total ~ 4.5–9 of all added ions, see ESI:† Note S4). This clearly illustrates, that a single encounter between a Ca^{2+}-carrying and a CO_3^{2-}-carrying reverse micelles would by no means yield a solid phase, although the concentration of ions was significantly above saturation for ACC, vaterite, calcite or aragonite (see Experimental). On the other hand, it has been recently demonstrated that the calcium and carbonate ions show high mutual affinity and will form stable solute ionic associates in solution upon encounter even at highly undersaturated conditions.[44–47] These associates might be akin to the concept of the pre-nucleation clusters observed by Gebauer et al.,[44] but could very well be ion pairs.[47] Based mainly on the molecular modelling data supported by the indirect, yet consistent experimental evidence, the pre-nucleation clusters are suggested to have a form of small dynamically ordered liquid-like oxyanion polymers built of several Ca^{2+} and CO_3^{2-} ions.[45,46,48–50] Regardless of the actual form of speciation in solution, either poly-ionic or simpler, it is important to note that up to $\sim 75\%$ of calcium becomes bound in solution before nucleation of the solid phases.[47,51] Thus, our observations could be explained in terms of a selective accumulation of such small $CaCO_3$ solute species in the water cores of the reverse micelles. It has been established that in NaAOT-based microemulsion systems even small amounts of ionic species in the water pools can affect the stability and reactivity of reverse micelles.[52,53] Furthermore, with increasing salt concentrations inter-micellar attraction is attenuated, leading to micelles behaving more like hard-spheres, and increasing the stiffness of the surfactant interface.[38] Therefore, an increase in the electrolyte concentration should lead to a decrease in the reactivity of the microemulsion environment, and a decreased tendency to form clusters/aggregates of micelles.[54] On the other hand, lower ionic strengths inside the water cores should favor mixing of the water core contents, and formation of large clusters of micelles. In our case, we start with two initial microemulsions, which are stable. The presence of the dissolved ions impedes to a certain degree the overall communication between the aqueous cores upon mixing, yet, the actual ionic exchange processes occurs, but at lower probabilities of effective fusion–fission (Fig. 5A). Since we know that the formation of globules is caused by the inter-micellar communication, the rate of ion exchange should be correlated with the rate of globule growth. In other words, the globules should form faster at lower initial ion concentrations at a constant water-to-surfactant ratio w (i.e., equivalent size and number density of micelles). We tested this hypothesis by following the formation of globules using changes in the optical turbidity of mixed samples as a function of time at three different total ion concentrations (between 0.05 mol L^{-1} and 0.1 mol L^{-1} with respect to $CaCO_3$) but all at $w = 10$. The comparison (ESI:† Fig. S6) shows that the globules form indeed at faster rates for lower ion concentrations, supporting our hypothesis. Our data suggest that as the ionic exchange progresses through fusion–fission (Fig. 5B), Ca–CO_3 solute species form. Consequently, the effective ionic strength in the aqueous

This journal is © the Owner Societies 2018

Phys. Chem. Chem. Phys., 2018, 20, 13825–13835 | 13831

Fig. 5 Schematics of the microemulsion processes leading to the formation of globules followed by the induced solid $CaCO_3$ formation. (A) Initial state and mixing of two ion-carrying microemulsions. In NaAOT-based microemulsion systems[19,54] where salt ions are present the chemical exchange/communication between the aqueous ion-containing water-cores is partially impeded. In general, at raising salt concentrations, the effective polar head area of the NaAOT surfactant decreases, due to the screening by any additional ions, which also leads to a decrease in the repulsion between the heads. Therefore, the presence of salts causes the surfactant packing parameter[54] v/al (where v is an effective volume of a NaAOT molecule, l length of the nonpolar tail) to increase. This salt-induced increase in v/al translates into a simultaneous increase in the stiffness of the surfactant interface and this in turn hinders percolation and ion exchange between the individual micelles. As a consequence, any opening of inter-droplet channels and exchange of water core contents is less likely.[54] On the other hand, lower salinities (relative to starting conditions) favor "sticky" dynamic interactions, and the formation of large micellar globular aggregates; (B) inter-micellar interaction and ion-exchange, driving the formation of stable liquid-like Ca–CO_3 species (possibly akin to ion pairs or prenucleation clusters[44]); (C) formation of clusters of micelles containing stabilized Ca–CO_3 species (i.e., low salinity and hence "sticky"), surrounded by a "sea" of hard-sphere-like micelles containing primarily dissociated counter ions (i.e., high salinity); (D) destabilization through the breakdown of the surfactant interface due to the presence of ethanol, followed by the unrestricted merging of water core contents, and the rapid association of small Ca–CO_3 species in the aqueous phase leading to the precipitation of solid $CaCO_3$. The aggregates in C and D are schematic, since the actual observed morphologies (Fig. 2) include tens of thousands of aggregated/clustered micelles.

cores will decrease as increasingly more ions become associated with each other. Thus, the surfactant interface of micelles containing Ca–CO_3 species becomes less stiff, and such micelles likely show higher tendencies to cluster/aggregate into globules (Fig. 5C). This decrease in stiffness and increase in the tendency to form globules is also reflected by a small decrease in the volume of the individual micelles observed during the reaction (5% after 180 min; Fig. 1), which is expected for the transition to a more fluid surfactant interface.[19] According to the model of solubilization of small molecules,[19] the decrease in micellar radius and the decrease of stiffness of the micelle interfaces should occur when the solute molecules are directly anchored to such interfaces. In our system, this results in a population of micelles that do not (practically) contain Ca–CO_3, in their water cores (Fig. 5B) but instead primarily contain dissociated Na^+ and Cl^- ions (Fig. 5C at right) that contribute to the relatively

increased salinity in the water pools. Hence, this second population of micelles is effectively less "sticky" and does not easily form aggregated globules. In experiments that utilize purely inorganic aqueous solutions, amorphous calcium carbonate (ACC) is the first solid phase that precipitates from bulk solution[41,55] Its formation, stability and subsequent transformation to crystalline $CaCO_3$ phases is highly dependent on variations in physicochemical properties of the systems observed.[39–42] In contrast, in our microemulsions we do not have a bulk homogenous solution. Instead each individual microemulsion micelle has a highly confined volume and is less than 4 nm in diameter. Models and experiments suggest that highly confined volumes (e.g., nanopores) can contain solutions at higher supersaturations when compared to unconfined bulk conditions (i.e., pore-size controlled solubility effect, where an effective solubility is defined for confined volumes, following the Young–Laplace equation[56–59]). Furthermore, recent studies[60,61] have shown that highly hydrophilic substrates are not good templates for heterogeneous nucleation, due to the high energetic barriers associated to surface dehydration. Assuming therefore that the highly hydrophilic inner surfaces of micelles do not provide a good substrate for heterogeneous nucleation, the effective solubility becomes the most important thermodynamic parameter controlling homogeneous nucleation in the micelle-water system. Applying the Young–Laplace equation[56,57] to a micellar water pool of 4 nm predicts that the effective solubility of $CaCO_3$ (calcite) under such confinement is ~3.5 times higher than the bulk solubility of macro-crystalline calcite. This suggests that within the confinement of our <4 nm sized micellar water cores and considering the highly limited temporal and spatial availability of ions, the precipitation of a solid inside such water cores is far less favorable than in the bulk. At the same time however, it was shown that very e.g. small $CaCO_3$ clusters/species (1.4 nm) can be stabilized by organic ligands such as 10,12-pentacosadiynoic acid.[62] This is likely also the reason why in our experiments, the microemulsion environment similarly hinders the formation of solid $CaCO_3$ phases and favors the stabilization of small clusters/species. We could induce crystallization only upon the bursting of the globular aggregates following the addition of ethanol (Fig. 3) because this led to the rapid removal of the confinement and to the fast decrease in the stabilizing properties of the micellar interface. The injection of ethanol (Fig. 3 and ESI:† Video S2) perturbs near-instantaneously the surfactant film and destabilizes the water droplets and hence also the ions inside the globules (ESI:† Fig. S2B, C and S3). This disruption naturally leads to instant phase separation and disintegration of the globules followed by the fast growth of solid $CaCO_3$ from the supersaturated aggregated globular liquid-like Ca–CO_3 phase (Fig. 5D).

Conclusions

Our results highlight a strong feedback between the changing state of the interacting ionic species in the water cores and the structure/composition/interfaces of the reverse micelles themselves. The proposed stabilization and 'triggered' destabilization mechanisms

13832 | Phys. Chem. Chem. Phys., 2018, 20, 13825–13835

This journal is © the Owner Societies 2018

are examples of nano-scale mediated mineral nucleation and growth process. The organic interface–inorganic species interactions compete with the purely inorganic drivers changing the thermodynamics of the system, where only in the presence of a stable micellar interface, the solute Ca–CO$_3$ species could be preserved within clusters/aggregates (the globules) of reverse micelles. This is in stark contrast to non-micellar fully inorganic aqueous systems, where solids form instantaneously at the same chemical conditions. Finally, only when a perturbation was introduced by ethanol addition, did the micellar interface become unstable, allowing for the unhindered mixing of the aqueous phases and their contents, and consequently lead to vaterite crystallization.
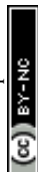
Conflicts of interest

There are no conflicts of interest to declare.

Acknowledgements

References

1 J. D. Milliman, Production and accumulation of calcium carbonate in the ocean: Budget of a nonsteady state, *Global Biogeochem. Cycles*, 1993, **7**, 927–957.

2 A. B. Hastings, C. D. Murray and J. Sendroy, Studies of the solubility of calcium salts I. The solubility of calcium carbonate in salt solutions and biological fluids, *J. Biol. Chem.*, 1927, **71**, 723–781.

3 J. Johnston, The several forms of calcium carbonate, *Am. J. Sci.*, 1916, **61**, 473–512.

4 J. J. De Yoreo, P. U. P. A. Gilbert, N. A. J. M. Sommerdijk, R. L. Penn, S. Whitelam, D. Joester, H. Zhang, J. D. Rimer, A. Navrotsky, J. F. Banfield, A. F. Wallace, F. M. Michel, F. C. Meldrum, H. Colfen and P. M. Dove, Crystallization by particle attachment in synthetic, biogenic, and geologic environments, *Science*, 2015, **349**, aaa6760.

5 S. Mann and G. A. Ozin, Synthesis of inorganic materials with complex form, *Nature*, 1996, **382**, 313–318.

6 H. Cölfen and M. Antonietti, Crystal design of calcium carbonate microparticles using double-hydrophilic block copolymers, *Langmuir*, 1998, **14**, 582–589.

7 M.-P. Pileni, The role of soft colloidal templates in controlling the size and shape of inorganic nanocrystals, *Nat. Mater.*, 2003, **2**, 145–150.

8 D. G. Shchukin and G. B. Sukhorukov, Nanoparticle Synthesis in Engineered Organic Nanoscale Reactors, *Adv. Mater.*, 2004, **16**, 671–682.

9 M. Li and S. Mann, Emergent Nanostructures: Water-Induced Mesoscale Transformation of Surfactant-Stabilized Amorphous Calcium Carbonate Nanoparticles in Reverse Microemulsions, *Adv. Funct. Mater.*, 2002, **12**, 773–779.

10 P. J. M. Smeets, K. R. Cho, R. G. E. Kempen, N. A. J. M. Sommerdijk and J. J. De Yoreo, Calcium carbonate nucleation driven by ion binding in a biomimetic matrix revealed by in situ electron microscopy, *Nat. Mater.*, 2015, **4193**, 1–6.

11 C. C. Tester, R. E. Brock, C.-H. Wu, M. R. Krejci, S. Weigand and D. Joester, In vitro synthesis and stabilization of amorphous calcium carbonate (ACC) nanoparticles within liposomes, *CrystEngComm*, 2011, **13**, 3975–3978.

12 C. C. Tester, C.-H. Wu, S. Weigand and D. Joester, Precipitation of ACC in liposomes—a model for biomineralization in confined volumes, *Faraday Discuss.*, 2012, **159**, 345–356.

13 M. P. Pileni, Nanosized Particles Made in Colloidal Assemblies, *Langmuir*, 1997, **13**, 3266–3276.

14 D. E. Moilanen, E. E. Fenn, D. Wong and M. D. Fayer, Water dynamics in large and small reverse micelles: From two ensembles to collective behavior, *J. Chem. Phys.*, 2009, **131**, 14704.

15 G. Onori and A. Santucci, Ir Investigations of Water-Structure in Aerosol Ot Reverse Micellar Aggregates, *J. Phys. Chem.*, 1993, **97**, 5430–5434.

16 V. Uskoković and M. Drofenik, Reverse micelles: Inert nano-reactors or physico-chemically active guides of the capped reactions, *Adv. Colloid Interface Sci.*, 2007, **133**, 23–34.

17 K. Martinek, N. L. Klyachko, A. V. Kabanov, Y. L. Khmelnitsky and A. V. Levashov, Micellar enzymology: its relation to membranology, *Biochim. Biophys. Acta, Biomembr.*, 1989, **981**, 161–172.

18 U. Natarajan, K. Handique, A. Mehra, J. R. Bellare and K. C. Khilar, Ultrafine Metal Particle Formation in Reverse Micellar Systems: Effects of Intermicellar Exchange on the Formation of Particles, *Langmuir*, 1996, **12**, 2670–2678.

19 M. P. Pileni, Reverse micelles as microreactors, *J. Phys. Chem.*, 1993, **97**, 6961–6973.

20 H. Eicke, J. C. Shepherd and A. Steinemann, Exchange of solubilized water and aqueous electrolyte solutions between micelles in apolar media, *J. Colloid Interface Sci.*, 1976, **56**, 168–176.

21 J. Eastoe, M. J. Hollamby and L. Hudson, Recent advances in nanoparticle synthesis with reversed micelles, *Adv. Colloid Interface Sci.*, 2006, **128–130**, 5–15.

This journal is © the Owner Societies 2018

Phys. Chem. Chem. Phys., 2018, **20**, 13825–13835 | 13833

22 F. Rauscher, P. Veit and K. Sundmacher, Analysis of a technical-grade w/o-microemulsion and its application for the precipitation of calcium carbonate nanoparticles, *Colloids Surf., A*, 2005, **254**, 183–191.

23 S. H. Kang, I. Hirasawa, W.-S. Kim and C. K. Choi, Morphological control of calcium carbonate crystallized in reverse micelle system with anionic surfactants SDS and AOT, *J. Colloid Interface Sci.*, 2005, **288**, 496–502.

24 C. Y. Tai and C. Chen, Particle morphology, habit, and size control of $CaCO_3$ using reverse microemulsion technique, *Chem. Eng. Sci.*, 2008, **63**, 3632–3642.

25 H.-S. Liu, K.-A. Chen and C. Y. Tai, Droplet stability and product quality in the Higee-assisted microemulsion process for preparing $CaCO_3$ particles, *Chem. Eng. J.*, 2012, **197**, 101–109.

26 C.-K. Chen and C. Y. Tai, Competing effects of operating variables in the synthesis of $CaCO_3$ particles using the reverse microemulsion technique, *Chem. Eng. Sci.*, 2010, **65**, 4761–4770.

27 B. Tamamushi and N. Watanabe, The formation of molecular aggregation structures in ternary system: Aerosol OT/water/iso-octane, *Colloid Polym. Sci.*, 1980, **258**, 174–178.

28 T. C. Huang, H. Toraya, T. N. Blanton and Y. Wu, X-ray powder diffraction analysis of silver behenate, a possible low-angle diffraction standard, *J. Appl. Crystallogr.*, 1993, **26**, 180–184.

29 P. Fratzl, K. Misof, I. Zizak, G. Rapp, H. Amenitsch and S. Bernstorff, Fibrillar Structure and Mechanical Properties of Collagen, *J. Struct. Biol.*, 1998, **122**, 119–122.

30 F. Zhang, J. Ilavsky, G. G. Long, J. P. G. Quintana, A. J. Allen and P. R. Jemian, Glassy Carbon as an Absolute Intensity Calibration Standard for Small-Angle Scattering, *Metall. Mater. Trans. A*, 2010, **41**, 1151–1158.

31 M. Basham, J. Filik, M. T. Wharmby, P. C. Y. Chang, B. El Kassaby, M. Gerring, J. Aishima, K. Levik, B. C. A. Pulford, I. Sikharulidze, D. Sneddon, M. Webber, S. S. Dhesi, F. Maccherozzi, O. Svensson, S. Brockhauser, G. Náray and A. W. Ashton, Data Analysis WorkbeNch (DAWN), *J. Synchrotron Radiat.*, 2015, **22**, 853–858.

32 M. E. Holtz, Y. Yu, H. D. Abruña and D. A. Muller, *In situ* Electron Energy Loss Spectroscopy of Liquids, *Microsc. Microanal.*, 2012, **18**, 1094–1095.

33 A. P. Hammersley, S. O. Svensson, M. Hanfland, A. N. Fitch and D. Hausermann, Two-dimensional detector software: From real detector to idealised image or two-theta scan, *High Press. Res.*, 1996, **14**, 235–248.

34 P. Juhás, T. Davis, C. L. Farrow and S. J. L. Billinge, PDFgetX3: A rapid and highly automatable program for processing powder diffraction data into total scattering pair distribution functions, *J. Appl. Crystallogr.*, 2013, **46**, 560–566.

35 R. Hilfiker, H. F. Eicke, W. Sager, C. Steeb, U. Hofmeier and R. Gehrke, Form and structure factors of water/AOT/oil microemulsions from synchrotron SAXS, *Berichte der BunsenGesellschaft*, 1990, **94**, 677–683.

36 I. Bressler, B. R. Pauw and A. F. Thünemann, McSAS: software for the retrieval of model parameter distributions from scattering patterns, *J. Appl. Crystallogr.*, 2015, **48**, 962–969.

37 R. Itri, C. L. C. Amaral and M. J. Politi, Interactive forces on Aerosol-OT/n-hexane/water/urea reversed micelles by small angle x-ray scattering, *J. Chem. Phys.*, 1999, **111**, 7668–7674.

38 J. S. Huang, Surfactant interactions in oil continuous microemulsions, *J. Chem. Phys.*, 1985, **82**, 480–484.

39 M. H. Nielsen, S. Aloni and J. J. De Yoreo, In situ TEM imaging of CaCO3 nucleation reveals coexistence of direct and indirect pathways, *Science*, 2014, **345**, 1158–1162.

40 Z. Zou, L. Bertinetti, Y. Politi, A. C. S. Jensen, S. Weiner, L. Addadi, P. Fratzl and W. J. E. M. Habraken, Opposite Particle Size Effect on Amorphous Calcium Carbonate Crystallization in Water and during Heating in Air, *Chem. Mater.*, 2015, **27**, 4237–4246.

41 P. Bots, L. G. Benning, J.-D. Rodriguez-Blanco, T. Roncal-Herrero and S. Shaw, Mechanistic Insights into the Crystallization of Amorphous Calcium Carbonate (ACC), *Cryst. Growth Des.*, 2012, **12**, 3806–3814.

42 J. D. Rodriguez-Blanco, S. Shaw and L. G. Benning, The kinetics and mechanisms of amorphous calcium carbonate (ACC) crystallization to calcite, via vaterite, *Nanoscale*, 2011, **3**, 265–271.

43 D. J. Tobler, J. D. Rodriguez-Blanco, K. Dideriksen, N. Bovet, K. K. Sand and S. L. S. Stipp, Citrate Effects on Amorphous Calcium Carbonate (ACC) Structure, Stability, and Crystallization, *Adv. Funct. Mater.*, 2015, **25**, 3081–3090.

44 D. Gebauer, A. Völkel and H. Cölfen, Stable prenucleation calcium carbonate clusters, *Science*, 2008, **322**, 1819–1822.

45 R. Demichelis, P. Raiteri, J. D. Gale, D. Quigley and D. Gebauer, Stable prenucleation mineral clusters are liquid-like ionic polymers, *Nat. Commun.*, 2011, **2**, 1–8.

46 M. Kellermeier, P. Raiteri, J. Berg, A. Kempter, J. Gale and D. Gebauer, Entropy drives calcium carbonate ion association, *ChemPhysChem*, 2016, **17**, 3535–3541.

47 P. J. M. Smeets, A. R. Finney, W. J. E. M. Habraken, F. Nudelman, H. Friedrich, J. Laven, J. J. De Yoreo, P. M. Rodger and N. A. J. M. Sommerdijk, A classical view on nonclassical nucleation, *Proc. Natl. Acad. Sci. U. S. A.*, 2017, 201700342.

48 P. Raiteri, R. Demichelis, J. D. Gale, M. Kellermeier, D. Gebauer, D. Quigley, L. B. Wright and T. R. Walsh, Exploring the influence of organic species on pre- and post-nucleation calcium carbonate, *Faraday Discuss.*, 2012, **159**, 61.

49 M. A. Bewernitz, D. Gebauer, J. Long, H. Cölfen and L. B. Gower, A metastable liquid precursor phase of calcium carbonate and its interactions with polyaspartate, *Faraday Discuss.*, 2012, **159**, 291.

50 M. Kellermeier, A. Picker, A. Kempter, H. Cölfen and D. Gebauer, A Straightforward Treatment of Activity in Aqueous $CaCO_3$ Solutions and the Consequences for Nucleation Theory, *Adv. Mater.*, 2014, **26**, 752–757.

51 D. Gebauer, M. Kellermeier, J. D. Gale, L. Bergström and H. Cölfen, Pre-nucleation clusters as solute precursors in crystallisation, *Chem. Soc. Rev.*, 2014, **43**, 2348–2371.

52 B. Bedwell and E. Gulari, Electrolyte-moderated interactions in water/oil microemulsions, *J. Colloid Interface Sci.*, 1984, **102**, 88–100.

13834 | *Phys. Chem. Chem. Phys.*, 2018, **20**, 13825–13835

This journal is © the Owner Societies 2018

53 J. J. Silber, A. Biasutti, E. Abuin and E. Lissi, Interactions of small molecules with reverse micelles, *Adv. Colloid Interface Sci.*, 1999, **82**, 189–252.

54 L. Garcia-Rio, J. Leis, J. Mejuto, M. Pena and E. Iglesias, Effects of additives on the internal dynamics and properties of water/AOT/isooctane microemulsions, *Langmuir*, 1994, **10**, 1676–1683.

55 J. D. Rodriguez-Blanco, S. Shaw and L. G. Benning, How to make 'stable' ACC: protocol and preliminary structural characterization, *Mineral. Mag.*, 2008, **72**, 283–286.

56 G. W. Scherer, Crystallization in pores, *Cem. Concr. Res.*, 1999, **29**, 1347–1358.

57 S. Emmanuel and J. J. Ague, Modeling the impact of nanopores on mineralization in sedimentary rocks, *Water Resour. Res.*, 2009, **45**, 1–12.

58 A. Putnis, M. Prieto and L. Fernandez-Diaz, Fluid supersaturation and crystallization in porous media, *Geol. Mag.*, 1995, **132**, 1.

59 J. Zachara, S. Brantley, J. Chorover, R. Ewing, S. Kerisit, C. Liu, E. Perfect, G. Rother and A. G. Stack, Internal Domains of Natural Porous Media Revealed: Critical Locations for Transport, Storage, and Chemical Reaction, *Environ. Sci. Technol.*, 2016, **50**, 2811–2829.

60 A. Fernandez-Martinez, Y. Hu, B. Lee, Y.-S. Jun and G. A. Waychunas, In Situ Determination of Interfacial Energies between Heterogeneously Nucleated $CaCO_3$ and Quartz Substrates: Thermodynamics of CO_2 Mineral Trapping, *Environ. Sci. Technol.*, 2013, **47**, 102–109.

61 C. Dai, A. G. Stack, A. Koishi, A. Fernandez-Martinez, S. S. Lee and Y. Hu, Heterogeneous Nucleation and Growth of Barium Sulfate at Organic–Water Interfaces: Interplay between Surface Hydrophobicity and Ba2+ Adsorption, *Langmuir*, 2016, **32**, 5277–5284.

62 S. Sun, D. Gebauer and H. Cölfen, A solvothermal method for synthesizing monolayer protected amorphous calcium carbonate clusters, *Chem. Commun.*, 2016, **52**, 7036–7038.

This journal is © the Owner Societies 2018

Phys. Chem. Chem. Phys., 2018, **20**, 13825–13835 | **13835**